Chapter 3: A Pair Distribution Function Study of Ni₂MnGa Magnetic Shape Memory Alloy: Evidence for the Precursor State of the Premartensite Phase

This chapter contains the evidence for the precursor state of the premartensite phase in Ni₂MnGa magnetic shape memory alloy using magnetic measurements and atomic pair distribution function (PDF) analysis of high-energy, high-flux, and high-Q synchrotron x-ray powder diffraction data.

3.1 Introduction

Martensite transition is a diffusionless displacive phase transition where atoms in the high symmetry cubic austenite phase move in a cooperative manner to lower the symmetry and give rise to a martensite phase with specific microstructural features [14-16, 18]. This transition forms the basis of the development of several technologically important ferrous and non-ferrous alloys with applications ranging from the ground, marine, and aerospace structures to biomedical implants, energy conversion devices, actuators, and smart structures, to name just a few [14-16]. Martensite transitions are ubiquitous and have been observed in a different class of materials, including elemental metals (Co and group IV metals like Ti, Zr, etc.) [20, 21], ferrous and non-ferrous alloys [14-16, 248], superconducting A-15 alloys [249], ceramics [15, 16], oxides (ZrO₂) [22], sulphides (ZnS) [23], organometallic compounds [250], aminoacids [25, 26], and block copolymer micelles [24]. Martensite transition was first discovered in steels, where it is irreversible and athermal [14]. In contrast, the temperature and/or stress-induced martensite transitions in shape memory alloys (SMAs) like Ni-Ti [14-16, 27, 28], Ni-Al [14, 29, 30], and Cu-based alloys (like Cu-Zn-Al, Cu-Al-Ni, etc.) [16, 251], and magnetic shape memory alloys (MSMAs) like Ni-Mn-Ga [1, 35, 36] are reversible and may have both athermal [14, 31, 252, 253] and isothermal [14, 16, 31, 253-255] characteristics depending on the alloy system. The martensite transition is at

the heart of the large and reversible shape change in the SMAs wherein different orientational variants of the martensite phase, formed by twinning to maintain the invariant habit plane, merge on the application of stress while the original austenite state is recovered by heating to the austenite phase region [14-16]. The MSMAs have advantage over conventional SMAs as they provide much larger strains not only under the influence of temperature and stress but also on application of magnetic field which gives faster actuation within the martensite phase itself but the brittleness of the alloys is still an issue of intense research [1, 2, 13, 35-38].

Even though the shape change in the SMAs on the application of temperature or stress (or magnetic field in MSMAs) is due to the martensite phase transition, the martensite phase in the important SMAs exhibiting large strains does not result directly from the high-temperature cubic austenite phase but is preceded by an intermediate premartensite phase [14, 16, 63, 99, 109, 112-114]. As a result, the precursor phenomena in SMAs and MSMAs have received enormous attention from the point of view of phonon softening, crystal structure, phase stabilities, and physical properties [63, 88, 99, 109, 112-124]. The precursor state in nearly stoichiometric or off-stoichiometric Ni-Ti or Fe-doped Ni-Ti [14, 16, 27, 112, 136] SMAs is characterized by the presence of diffuse scattering around the incommensurate positions of the trigonal structure (3R) [27, 74, 106, 137-140]. This state is labeled as the premartensite-I [106] state, which, at lower temperatures, is followed by the long-range ordered (LRO) R-phase, with a trigonal structure in the space group $P\bar{3}$ [28, 116], also labeled as premartensite-II [106] or R-martensite phase [27, 130, 131]. In the case of Ni-Mn-Ga based MSMAs, the premartensite phase is labeled as incommensurate $3M$ modulated structure (*Immm(00γ)s00* super-space group) with Burger orientation relationship $(110)_A \parallel (010)_{PM}$, $[110]_A \parallel [100]_{PM}$, $[1\bar{1}0]_A \parallel [001]_{PM}$, and $[001]_A \parallel [010]_{PM}$ for the lattice deformation shear[14, 63, 69-71, 256]. The austenite to premartensite phase transition has been linked with complete (as in Ni-Ti

SMA [27, 143, 257]) or partial softening (as in Ni_2MnGa MSMA) of the 1/3 (110) transverse acoustic (TA$_2$) mode with displacement along [1$\bar{1}$0] direction observed in inelastic neutron scattering studies [88, 118, 120, 121, 146]. In the case of Ni_2MnGa MSMA, there is also fermi surface nesting coupled to the soft mode that leads to Peierls like lattice distortions and opens a pseudogap at the new Brillouin zone boundary of the premartensite phase [90, 258].

Recent years have witnessed a lot of interest in understanding the precursor state of premartensite phase in the off-stoichiometric SMAs and MSMAs in relation to the occurrence of a fascinating strain-glass state [10, 124-132] which bears close analogy with spin-glasses [133], dipole glasses [134], and relaxors [135]. In this context, one of the most investigated systems is $Ti_{50}Ni_{50-x}Fe_x$, which for low concentrations of Fe shows austenite B2 phase to incommensurate premartensite-I phase (3R) to long-range ordered (LRO) commensurate R-phase (premartensite-II) to LRO martensite B19′ phase (monoclinic) transitions with decreasing temperature [106, 127, 129, 131]. Between the austenite and premartensite-II (R-phase) phase regions, the system shows a precursor state, comprising nanodomains of the 3R phase as hetero-phase fluctuations, whose stability regime widens with increasing Fe concentration until for x≥6 the formation of the LRO R- and B19′ phases are completely suppressed and only the short-range ordered (SRO) premartensite phase survives [127, 128, 131, 259]. The SRO premartensite phase exhibits locally fluctuating ferroelastic strains mimicking an ergodic "strain liquid state" whose characteristic time scale has been shown to diverge due to ergodic symmetry breaking at the strain-glass freezing temperature (T_g) when the disorder content, and hence frustration, exceeds a critical value [125-127, 259, 260].

The stoichiometric Ni_2MnGa MSMA shows a close similarity with the sequence of thermodynamic phase transitions discussed above in the context of $Ti_{50}Ni_{50-x}Fe_x$ SMA for x<5 [127, 131]. With decreasing temperature, the L2$_1$ ordered austenite phase of Ni_2MnGa undergoes

a first-order phase transition to LRO 3M modulated premartensite phase at $T_{PM} \sim 260$ K, which on further cooling undergoes a strong first-order phase transition to a 7M modulated martensite phase at $T_M \sim 210$ K [63, 69, 85]. Recent synchrotron x-ray powder diffraction (SXRPD) studies have confirmed the thermodynamic stability of the premartensite phase both in stoichiometric and 10% Pt substituted compositions unambigously [63, 123]. However, the signature of the precursor phenomena in the parent cubic austenite phase in the form of phonon softening in inelastic neutron scattering [118] and diffuse scattering in elastic neutron scattering [88] studies well above the T_{PM} necessitates a careful investigation of the local structure of Ni$_2$MnGa MSMA to understand the precursor state of the premartensite phase and its consequences on the magnetic phase transition in the cubic austenite phase.

In analogy with the SRO precursor state (3R) of the premartensite-II phase (R-phase) in the Ti$_{50}$Ni$_{50-x}$Fe$_x$ SMA [127, 131], this chapter provides the evidence for the SRO precursor state of the premartensite phase in the cubic austenite phase of Ni$_2$MnGa with local 3M like structure well above the T_{PM} and even above the paramagnetic to ferromagnetic (FM) transition temperature (T_C) using atomic pair distribution function (PDF) analysis. We show that the presence of such SRO precursor state of the premartensite phase produces strains, which couple with the ferromagnetic (FM) order parameter fluctuations around T_C and renormalize the coefficient of the fourth-order term in Landau expansion leading to first-order character of the paramagnetic to FM phase transition, as confirmed by the observation of characteristic thermal hysteresis in the paramagnetic to FM transition in heating and cooling cycles. We also show that the temperature dependence of the unit cell volume of the austenite phase deviates significantly below the FM T_C with respect to that in the paramagnetic austenite phase and that the excess volume scales quadratically with the FM order parameter, as expected for the magnetovolume effect [261, 262]. We argue that the

presence of the SRO precursor premartensite state in the FM phase is responsible for the reduction in the magnetization immediately below T_C, due to the higher magnetocrystalline anisotropy [263] of the premartensite phase, causing significant deviation from the $M \sim (T\text{-}T_C)^{1/2}$ type order parameter behavior expected for a second-order paramagnetic to FM phase transition [264, 265]. This SRO precursor state of the premartensite phase is analogous to the unfrozen strain-glass state or the so-called "strain liquid state" of $Ni_{50+x}Ti_{50-x}$ [260] with one significant difference. In $Ni_{50+x}Ti_{50-x}$ [260], the nanoscale domains in the "strain liquid state" do not transform to the LRO state while the SRO precursor state of the premartensite phase in the stochiometric Ni_2MnGa gradually grows on lowering the temperature and leads to the LRO premartensite phase below T_{PM}.

3.2 Experimental Section

The polycrystalline ingot with nominal composition Ni_2MnGa was prepared using the standard arc-melting technique [266]. The appropriate quantity of each constituent element with a minimum of 99.99% purity was melted several times to get uniform composition. The melt-cast ingot was annealed in a vacuum-sealed quartz ampoule (vacuum $\sim 10^{-6}$ mbar) at a temperature of 1100 K for three days to achieve further homogeneity and finally quenched in the ice-water mixture. The chemical composition of the sample was checked using the energy dispersive analysis of x-rays (EDAX) technique and found to be $Ni_{1.99}Mn_{1.01}Ga$, which is termed as Ni_2MnGa hereafter. A part of the annealed ingot was crushed into powder using a mortar pestle and sealed in the quartz ampoule under the argon atmosphere (first evacuated up to $\sim 10^{-6}$ mbar and then argon filled), followed by annealing at 773 K for 10 h to remove the residual stresses, if any, introduced during the grinding [148, 267-269]. These residual stresses free powder samples were used in the current study.

The dc magnetization measurements were carried out using a physical properties measurement system (Quantum Design), and ac susceptibility measurements were performed using SQUID-VSM (Quantum Design, MPMS). The ac susceptibility data were collected during the warming cycle on zero-field cooled (ZFCW), and field cooled (FCW) states and also during field cooling (FC) in the temperature range 2–400 K at 10 Oe (amplitude) and 333 Hz (frequency) with a temperature sweep rate of 2 K/minute. In the ZFCW protocol, the sample was cooled from 400 K (well above its FM T_C) down to 2 K in the absence of a magnetic field, and after that, the ac susceptibility was measured from 2 to 400 K during warming. Similarly, the data were collected in the FC and FCW cycles as well. DC magnetization data at 100 Oe field were also obtained in the temperature range 2–400 K under the ZFCW protocol using sweep rate of 4 K/min and in the temperature range 300–396 K under FC and FCW using sweep rate of 1 K/min. The temperature dependent synchrotron x-ray powder diffraction (SXRPD) measurements were carried out in the high-resolution as well as high-Q modes using high energy x-rays with a wavelength (λ) of 0.20706 Å at P02.1 beamline at PETRA-III DESY, Germany. For the SXRPD measurements, borosilicate capillaries were used as the sample container. The high-Q measurements were performed with a maximum instrumental Q-value ($Q_{maxinst}$) of 21.3 Å^{-1}. The high-Q data for empty borosilicate capillary was also recorded for the background subtraction required to convert the raw diffraction data into data from the sample only.

3.3   Atomic Pair Distribution Function Method

Atomic PDF technique, originally developed to investigate the local correlations (i.e., SRO structure) in the liquids and amorphous solids, has become a powerful tool for investigating the deviation from the average LRO structure at short-range length scales [270-272]. The PDF provides the probability of finding the pair of atoms separated at distance r [270]. It is a total

scattering method in which both the Bragg and diffuse scattering, due to LRO and SRO structures, respectively, contribute simultaneously to the total scattering structure function $S(Q)$ [270-272]. The atomic PDF is obtained using the PDFgetx3 program [273]. The steps (or algorithm) for the atomic PDF conversion are given below [273]:

First of all, the raw diffraction data, which is intensity (I) vs Q (or I(Q)), of the empty capillary are subtracted from the I(Q) of sample including capillary to get the I(Q) of the sample only, i.e., I(Q) (sample + capillary) − I(Q) (capillary) = I(Q) (sample). Here, Q is the magnitude of the scattering vector $\boldsymbol{Q} = \boldsymbol{k_i}\text{-}\boldsymbol{k_f}$, where $\boldsymbol{k_i}$ and $\boldsymbol{k_f}$ are the incident and reflected wave vectors, respectively. In the next step, there may be multiplicative ($a(Q)$) and additive ($b(Q)$) components too in the measured intensity $I_m(Q)$, i.e., $I_m(Q) = a(Q) I_c(Q)+b(Q)$, where $I_c(Q)$ is the coherent scattering intensity, which contains all the information of sample only. The $b(Q)$ term contains scattering from the air, multiple scattering, Compton scattering, while $a(Q)$ component has the absorption of x-ray within the sample, the polarization of x-ray. The $I_m(Q)$ can be converted into total scattering structure function ($S(Q)$) using the relation given as $S(Q) = \frac{I_m(Q) - \langle b(Q)^2 \rangle + \langle b(Q) \rangle^2}{\langle b(Q) \rangle^2}$, where b is the scattering power of the constituent atom. This implies that any error in $I_m(Q)$ by $a(Q)$ and $b(Q)$ will lead to an error in $S(Q)$ also. The $S(Q)$ should be asymptotic such that $S(Q)$ tends to 1 as Q tends to infinite. This leads to the oscillation around zero in the $\{S(Q) - 1\}$, which is related to reduced structure function $F(Q) = Q\{S(Q) - 1\}$. In the next step, to compensate for the error in $S(Q)$ from $I_m(Q)$, an additive factor (B(Q)) is considered/added in $S(Q)$. So, the measured $S(Q)$, can be defined as $S_m(Q)$ = $S(Q)$ + B(Q). This implies that the measured $F(Q)$, defined as $F_m(Q) = Q\{S(Q) - 1 + B(Q)\} =$ $F(Q) + Q$ B(Q). Subsequently, the B(Q) is modelled using n[th] order polynomial $P_n(Q)$. After that, $Q P_n(Q)$ is fitted with $F_m(Q)$ and subtracted from $F_m(Q)$ to get real $F(Q)$ from the sample only, i.e.,

$F(Q) = F_m(Q) - Q\,P_n(Q)$. Finally, the atomic PDF is obtained by taking the Fourier transform of $F(Q)$.

In the present case, the $S(Q)$ in the temperature range of 260 K to 400 K were obtained from the high-Q ($Q_{max} = 21$ Å^{-1}) SXRPD data after applying the standard normalization and background corrections to raw scattering data using the PDFgetx3 program as mentioned above [273]. The experimental reduced atomic PDF, i.e., $G(r)$, was obtained using the program PDFgetx3 by taking the Fourier transform of the reduced structure function $F(Q)$ in the Q range of Q_{min} to Q_{max} using the following equation:

$$G\,(r) = 4\pi r\,[\rho(r) - \rho_0] = \frac{2}{\pi} \int_{Q_{min}}^{Q_{max}} F(Q)\,sinQr\,dQ \dots (3.1)$$

Here, Q_{max} and Q_{min} are the maximum and minimum cut-offs, respectively for the magnitude of the scattering wave vector, $\rho(r)$ is the atomic number density, and ρ_0 is the average atomic number density [270-272]. A sixth-order polynomial was used for modeling the background while processing the raw data, which results in the value of r_{poly} to 0.9 Å during the Fourier transformation of $F(Q)$. The r_{poly} is the distance in real space up to which an unphysical signal could be present due to possible errors during background modeling by the program PDFgetx3 with the assumption that there are no higher-frequency aberrations in the raw data [273]. The structure refinement of the experimental atomic PDF was carried out in the direct space using the program PDFgui (PDFFIT2) [274], which is a promoted version of the program PDFFIT [275]. Since the present PDF data was collected using high energy (60 keV) synchrotron x-rays in the transmission mode, the x-rays could penetrate through the powder sample in the sample holder and provide information about the bulk behavior, unlike the TEM techniques used earlier in the context of precursor state studies on off-stoichiometric Ni-Ti and Ni-Al alloys which are sensitive to only thin regions of the sample near the surface [99, 105, 138-140, 276]. The use of the high

flux synchrotron x-ray data, on the other hand, gives an excellent signal-to-noise ratio, which is a prerequisite condition for obtaining reliable atomic PDF data. Finally, the high-Q SXRPD value helps us in minimizing the Fourier truncation ripples during Fourier transformation for obtaining the atomic PDF from the recorded high-Q data [270].

3.4 Results and Discussion

3.4.1 Magnetization

The temperature dependence of dc magnetization ($M(T)$) of Ni_2MnGa measured under an applied magnetic field of 100 Oe following the ZFCW protocol is shown in Figure 3.1(a). The abrupt rise in $M(T)$ around 210 K is due to the martensite to premartensite phase transition, and the small dip around 260 K is due to the premartensite to austenite phase transition (see the inset of Figure 3.1(a)). Further, a sharp drop in $M(T)$ around 371 K is due to the FM austenite to paramagnetic austenite phase transition at the Curie transition temperature, $T_C \sim 371$ K. For the determination of the characteristic transition temperatures more precisely, the ac-susceptibility data under the ZFCW, FC, and FCW protocols is also measured. The temperature dependence of the real part of ac-susceptibility ($\chi'(T)$), measured at a sweeping temperature rate of 2 K/minute, is shown in Figure 3.1(b). At the Curie transition temperature, $T_C \sim 371$ K for the FC cycle, there is a sharp increase in the $\chi'(T)$. On lowering the temperature further, a small drop in the $\chi'(T)$ is observed around the premartensite start transition temperature $PM_s^c \cong T_{PM} \cong 260$ K followed by a larger drop in $\chi'(T)$ at the martensite start transition temperature $M_s^c \cong T_M \cong 220$ K due to the increase in the magnetocrystalline anisotropy in the FM premartensite and martensite phases with respect to the FM austenite and premartensite phases, respectively, similar to that seen in Figure 3.1(a) [66, 141]. The nature of the $\chi'(T)$ curve in the FCW and FC protocols are similar, except that the characteristic transition temperatures during cooling (FC) are lower than those for the heating

(FCW) cycle, as expected for a first-order phase transition [63, 264, 277, 278]. The characteristic transition temperatures, austenite start (A_s), austenite finish (A_f), martensite start (M_s), and martensite finish (M_f), are $A_s \sim 210$ K, $A_f \sim 230$ K, $M_s \sim 220$ K, and $M_f \sim 190$ K, respectively.

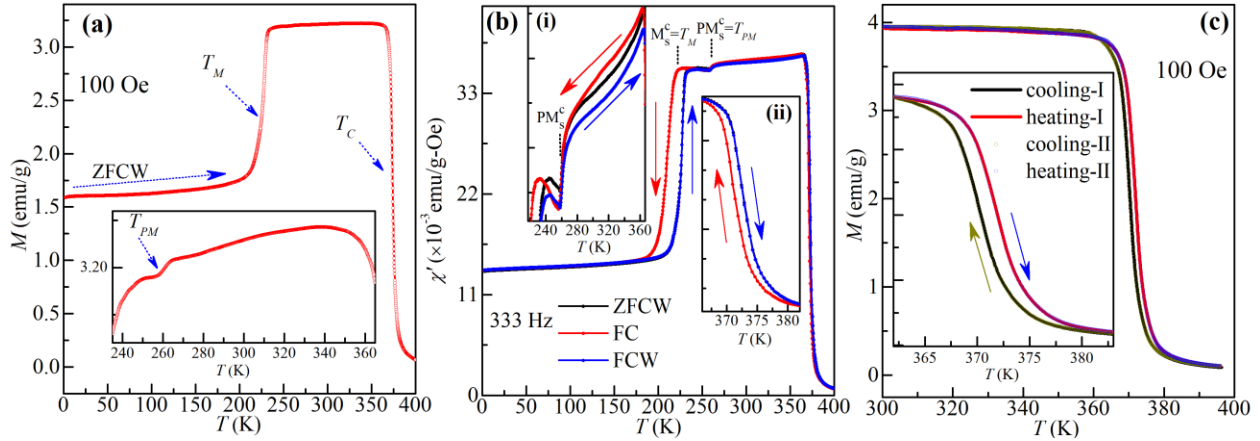Figure 3.1: Temperature dependence of the direct dc magnetization of Ni$_2$MnGa, measured at 100 Oe in the zero-field cooled warming (ZFCW) cycle at the rate of (a) 4 K/min and (c) 1 K/min and (b) temperature dependence of the real part of the ac-susceptibility of Ni$_2$MnGa measured at 333 Hz in the ZFCW (black color), field cooled (FC; red color), and field cooled warming (FCW; blue color) cycles. The inset of (a) gives an enlarged view for 235 K $\leq T \leq$ 365 K range to clearly show the dip in magnetization at the premartensite phase transition temperature $T_{PM} \sim 260$ K as well as the anomalously decreasing behavior of magnetization below the ferromagnetic (FM) Curie temperature (T_C). The insets (i) and (ii) of (b) show an enlarged view around the premartensite and FM transition temperatures, respectively. The inset of (c) shows the thermal hysteresis across FM T_C using two independent measurements labeled as I and II.

The difference between the temperatures (A_s+A_f)/2, obtained during heating for the FCW protocol, and (M_s+M_f)/2, obtained during cooling for the FC protocol, gives the thermal hysteresis of ~15 K due to the first-order nature of the martensite phase transition [14, 63, 85, 264]. A similar difference, though with a smaller value of thermal hysteresis (~2.4 K), in the characteristic

premartensite phase transition temperatures reveal the first-order character of the FM austenite to FM premartensite phase transition also. All the characteristic transition temperatures, determined from the $M(T)$ and $\chi'(T)$ plots, are in good agreement with those reported in the literature [63, 66, 69, 71, 120, 141, 148, 263, 279-281] .

There are two intriguing features observed in the $M(T)$ and $\chi'(T)$ plots. The first one is the thermal hysteresis in $\chi'(T)$ around T_C, which is shown on an expanded scale in the inset (ii) of Figure 3.1(b). The second one is a gradual decrease in the value of $M(T)$ below T_C with decreasing temperature, as shown on a magnified scale in the inset of Figure 3.1(a). The gradual drop in magnetization below T_C has also been reported in the single crystalline samples of Ni_2MnGa [282]. The dc magnetization, which is the order parameter for the paramagnetic austenite to the FM austenite transition, should keep on increasing, albeit slowly as $(T–T_C)^{1/2}$ [264, 265, 283]. Moreover, since paramagnetic to the FM phase transition is generally believed to be a second-order phase transition, one does not expect any thermal hysteresis around T_C in Ni_2MnGa also. To further confirm the appearance of thermal hysteresis around T_C, the $M(T)$ measurements at 100 Oe dc field were repeated several times around T_C with a slower temperature sweeping rate of 1 K/minute. The results of two such $M(T)$ measurements, labeled as I and II, are given in Figure 3.1(c) and in its inset in the cooling and heating sequence. In all these measurements, a thermal hysteresis of ~1.5 K around T_C (inset of Figure 3.1(c)) was reproduced. This indicates that the paramagnetic to FM phase transition has a first-order character in Ni_2MnGa. In addition, the Arrott plot, critical isotherm and universal curve analysis are also performed, in order to further confirm the first-order nature of the paramagnetic to FM phase transition in Ni_2MnGa MSMA. The detailed of Arrott plot, critical isotherm and universal curve analysis is given in following section.

3.4.2 Arrott Plot, Critical Isotherm and Universal Curve

3.4.2.1 Arrott Plot

The Arrott plot has been emerged as an excellent method to identify the order of the phase transition based on the Banerjee criterion [284-287]. Therefore, to get more insight into the thermal hysteresis observed around FM transition temperature ($T_C \sim 371$ K) in the temperature dependent magnetization (Figure 3.1(b) and (c)), the isothermal magnetization data were collected around T_C and shown in Figure 3.2(a), which exhibits ferromagnetic character below T_C. The Arrott plots were obtained from the isothermal magnetization and are shown in Figure 3.2(b). The Arrott plots exhibit a mainly positive slope besides only at the lower field region where the signature of the negative slope is clearly observed, as guided by the arrow in the inset of Figure 3.2(b) [285, 288]. Such a negative slope at the low field region in the Arrott plots is indication of the first-order phase transition [286]. Therefore, the appearance of a negative slope towards low field region in the Arrott plots suggesting the paramagnetic to FM phase transition in Ni_2MnGa MSMA is weak first-order in character. The critical isotherm, entropy change and universal curve analysis are given in the later section to get more information about the weak first-order character of magnetic transition in Ni_2MnGa MSMA.
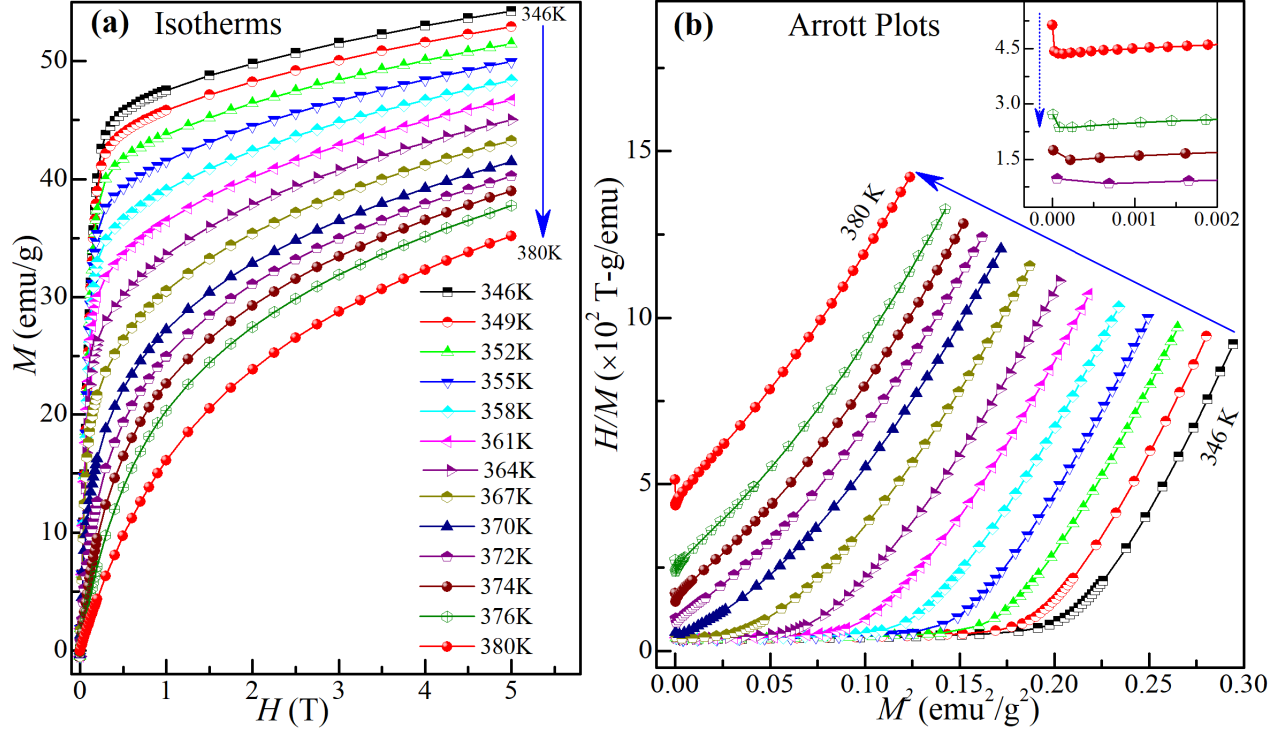
Figure 3.2: (a) The isothermal (magnetic field dependent) magnetization data around Curie temperature ($T_C \sim 371$ K). (b) The Arrott plots, obtained from (a). The inset of (b) shows the enlarged view around the lower field region, revealing the negative slope guided by a dotted blue arrow.

3.4.2.2 Critical Isotherm

The critical isotherm is the variation of $\ln(M)$ with $\ln(H)$ at the critical temperature, where M and H are magnetization and magnetic field, respectively. The critical isotherm is expected to be linear at the critical temperature for the second-order phase transition [289-292]. The $\ln(M)$ versus $\ln(H)$ plot (critical isotherm) around T_C for Ni$_2$MnGa MSMA is given in Figure 3.3, which clearly indicates the deviation from the linearity at lower magnetic field regions indicated by a wine-colored line, which is obtained by extrapolation of linearity fitted red line at 370 K (Figure 3.3). Although the critical isotherm has been reported linear for Ni$_2$MnGa MSMA, they have not reported the behavior at the lower magnetic field region [289]. The deviation at the lower field

regions in the present critical isotherm suggests the deviation from the ideal second-order magnetic phase transition. The universal curve analysis using magnetic entropy change is given in the next section to get detailed information about the present magnetic phase transition.
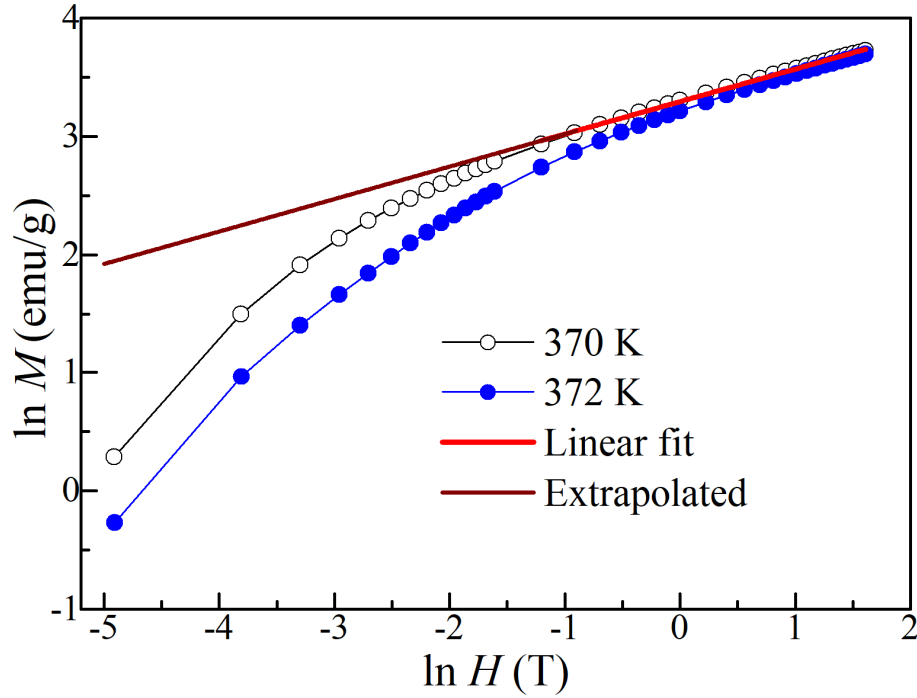

Figure 3.3: The behavior of ln(*M*) with ln(*H*) around $T_C \sim 371$ K. The red line represents the linear fitting at the higher field at 370 K. The significant deviation from the linearity at the lower magnetic field regions is indicated by extrapolated wine color line.

3.4.2.3 Magnetic Entropy Change and Universal Curve

The scaling of isothermal entropy change (ΔS_{iso}) in magnetocaloric materials has been adopted to study the critical phenomena and the nature of the magnetic phase transition [290, 292-294]. The isothermal field-dependent magnetization is used to calculate ΔS_{iso} using Maxwell equation [292] given as $\Delta S_{iso} = \mu_0 \int_0^H \left(\frac{\partial M}{\partial T}\right)_H dH$, where *M, H, T* and μ_0 are magnetization, magnetic field, temperature, and magnetic permeability of free space. The ΔS_{iso} was calculated for a different

70

magnetic field in the range of 0.01 to 5 T, as demonstrated in Figure 3.4. The peak point of ΔS_{iso} appears at a temperature around 371 K, which matches with T_C that appeared in the temperature dependent magnetization measurements (shown in Figure 3.1).
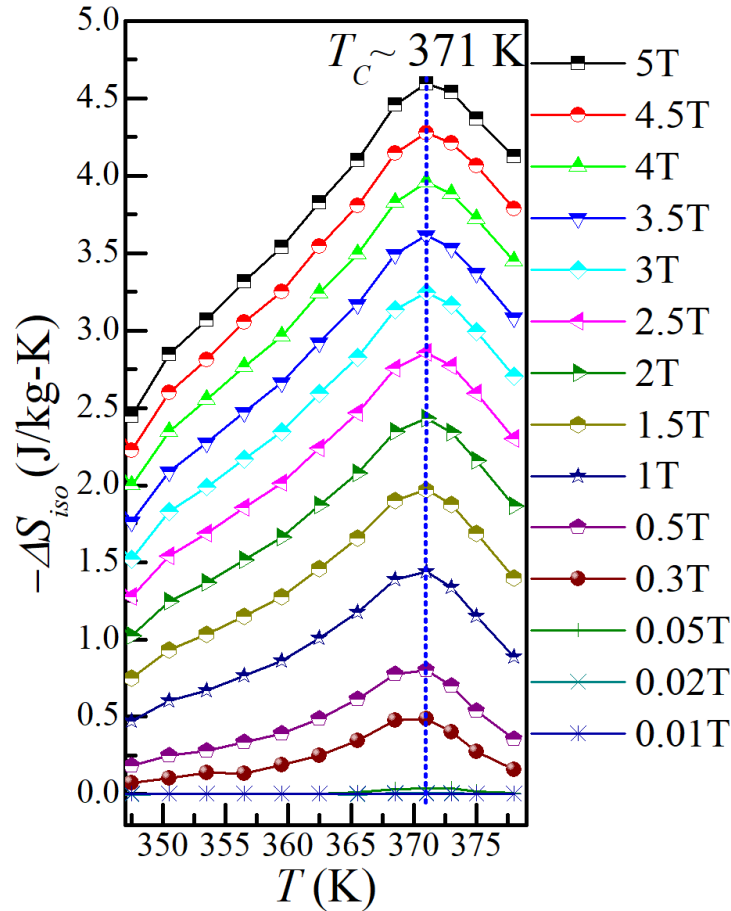

Figure 3.4: Isothermal entropy change versus temperature across the magnetic phase transition. The vertical dotted blue line marks the peak value, which appears at $T_C \sim 371$ K.

The variation of the peak value (ΔS_{pk}) of ΔS_{iso} with the magnetic field is shown in Figure 3.5 (a). The red line represents the fitting using the power law given by $\Delta S_{pk} = k\,H^n$, where k is a constant, H is the magnetic field, and n is an exponent [292, 295]. The fitting results value of $n \sim 0.73$, which is used to rescale the magnetic field axis by taking H^n and shown in Figure 3.5(b). The variation

71

of ΔS_{pk} with the rescaled magnetic field should be linear for the second-order phase transition as per the literature [287, 289]. However, Figure 3.5(b) exhibits a clear deviation from the linearity at the lower field region as guided by the blue line, suggesting the departure from the perfect second-order phase transition. This manifests the present paramagnetic to FM phase transition is not a perfect second-order. However, variation of ΔS_{pk} with rescaled the magnetic field has been reported linear for Ni_2MnGa MSMA [289], the behavior at lower magnetic field region has not been addressed.
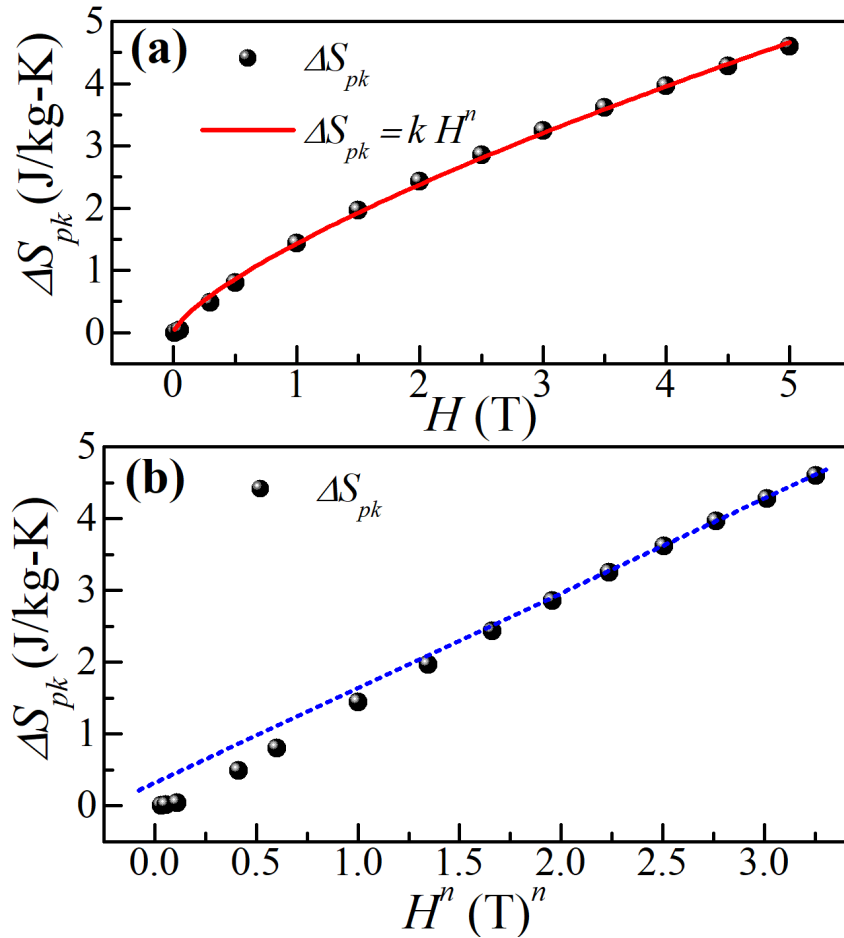

Figure 3.5: (a) The variation of the peak value of entropy change (ΔS_{pk}) (obtained from Figure 3.4) with change in the magnetic field. (b) The red line indicates the fit using power law ($\Delta S_{pk} = k\,H^n$).

The variation of ΔS_{pk} with the rescaled magnetic field (H^n). The blue line represents the deviation from linearity at the lower field region.

A universal curve analysis is performed to get more insight into the order of this FM transition because the universal curve using magnetic entropy change has been proposed to investigate the order of magnetic phase transitions in magnetocaloric materials [293-295]. First, the magnetic entropy change was normalized by dividing the ΔS_{iso} by its peak value, i.e., $\Delta S_{iso}/\Delta S_{pk}$, to construct the universal curve. After that, two reference points were used above and below T_C to scale the temperature axis using the following expression:

$$\theta = \begin{cases} -\dfrac{T-T_C}{T_{r1}-T_C}, & T \leq T_C \\ \dfrac{T-T_C}{T_{r2}-T_C}, & T > T_C \end{cases}$$

In the above expression, the T_{r1} and T_{r2} are the temperatures of two reference points such that they correspond to $\Delta S_{pk}/2$ below and above T_C, respectively [292-295]. The normalized entropy change ($\Delta S_{iso}/\Delta S_{pk}$) versus rescaled temperature (θ) is shown in Figure 3.6, which reveals that $\Delta S_{iso}/\Delta S_{pk}$ does not collapse on each other for $-0.5 > \theta > +0.5$, especially at low magnetic fields ($H < 1$ T). This suggests a deviation from second-order phase transition as for second-order phase transition, $\Delta S_{iso}/\Delta S_{pk}$ should collapse on a single curve [287, 293, 294, 296]. Therefore, the nonlinearity of critical isotherm (Figure 3.3), the nonlinearity of power law of entropy change (Figure 3.5(b)), and the absence of collapse on a single curve in the universal curve (Figure 3.6) indicate the deviation from ideal second-order behavior of paramagnetic to FM phase transition in Ni_2MnGa MSMA. The presence of small thermal hysteresis in temperature dependent magnetization measurement

around T_C (see Figure 3.1(b), Arrott plots (Figure 3.2(b)), and universal curve (Figure 3.6) analysis confirm the first-order character of paramagnetic to FM phase transition in Ni$_2$MnGa MSMA.
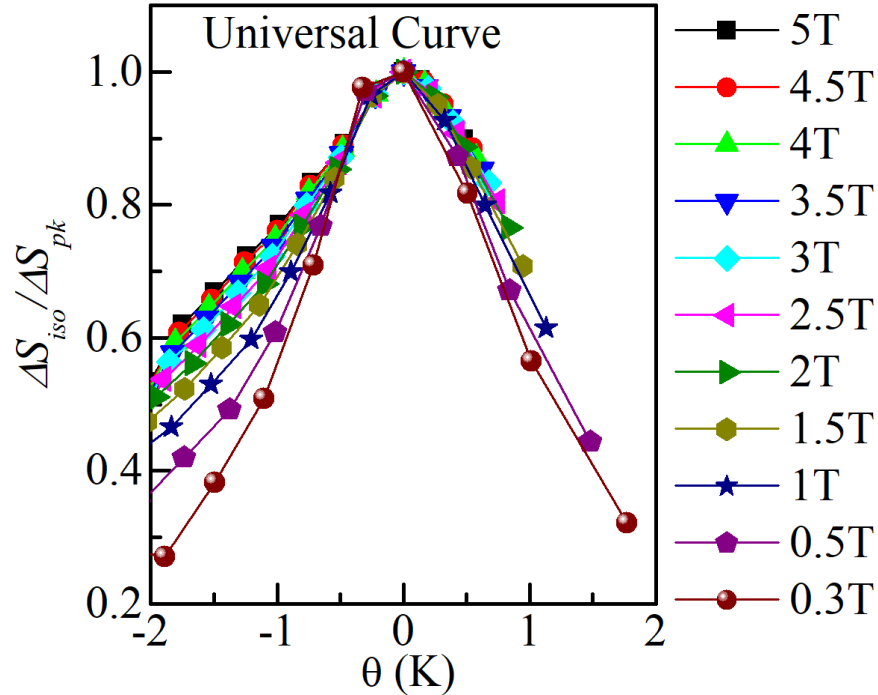

Figure 3.6: The normalized entropy change ($\Delta S_{iso}/\Delta S_{pk}$) versus rescaled temperature (θ)

The observation of thermal hysteresis (first-order nature) across T_C and the decrease in $M(T)$ at $T<$ T_C after its sharp jump around T_C (including the results of Arrott plots and universal curve) are not consistent with the conventional picture of a second-order paramagnetic to FM phase transition [264, 265, 297]. These observations encouraged us to perform a detailed temperature dependent structural studies above and below the T_C for the average and local structures using high-resolution and high-Q SXRPD data, respectively, to understand the genesis of the two unusual features in the magnetization studies.

3.4.3   Temperature Dependent High-Resolution Synchrotron X-ray Powder Diffraction

The high-resolution SXRPD patterns in the temperature range 260 K-400 K, shown in Figure *3.7*(a), do not reveal any signature of the structural phase transition above the premartensite phase transition temperature $T_{PM} \sim 260$ K. The increasing shift in the position of the most intense Bragg peak towards the lower 2θ side with increasing temperature, as shown in the inset (i) in Figure 3.7(a), is apparently due to the usual thermal expansion behavior. The satellite peaks appearing around the most intense cubic Bragg peak at $T \leq 260$ K, shown more clearly in the inset (ii) of Figure 3.7(a) at 260 K, correspond to the premartensite phase and are labeled as *"PM"* in the figure. The average long-range ordered structure was refined by the Rietveld technique [298] using the high-resolution SXRPD patterns. The refinement was carried out using the FULLPROF package [299]. For the refinement of the structure of the cubic austenite phase in the $Fm\bar{3}m$ space group, all the atoms were considered at special positions, i.e. Ni at 8c (0.25 0.25 0.25) and (0.75 0.75 0.75), Mn at 4a (0 0 0), and Ga at 4b (0.5 0.5 0.5) Wyckoff positions, respectively [69]. It was verified by Rietveld refinement that all the Bragg peaks above T_C as well in the temperature $T_{PM} < T \leq T_C$ in the SXRPD patterns is well accounted by the cubic austenite phase with the $Fm\bar{3}m$ space group. The Rietveld fits at 400 K ($>T_C$) and at 270 K ($T_{PM} < T < T_C$) are shown in Figure *3.7*(b) and (c), respectively. The refined lattice parameters are $a = 5.83064(3)$ Å and $5.81820(9)$ Å at 400 K and 270 K, respectively, which are in good agreement with those reported in the literature [63]. The variation of the unit cell volume (V), obtained from the Rietveld refinements, with temperature, shows a linear dependence on temperature for $T < 370$ K and $T \geq 370$ K, as can be seen from Figure 3.8(a). However, the slope of V versus T changes around the FM $T_C \sim 371$ K (see Figure 3.8(a)) obtained from the $M(T)$ and $\chi'(T)$ plots given in Figure 3.1(a) and Figure 3.1(b), respectively. The volume thermal expansion coefficient (TEC), defined as the ratio of change in

volume (ΔV), say from V to $V+\Delta V$, on increasing the temperature, say from T to $T+\Delta T$, to the change in temperature (ΔT) per unit the initial volume V at T, i.e., $\alpha_V (T) = \frac{\Delta V}{V*\Delta T}$ [300], was calculated from the temperature dependence of the unit cell volume, obtained by Rietveld refinement using the SXRPD data. It is interesting to note that the α_V exhibits a jump-like feature around T_C, as shown in Figure 3.8(b). This feature is similar to that obtained using strain gauge measurements for the linear TEC on Ni_2MnGa [301].
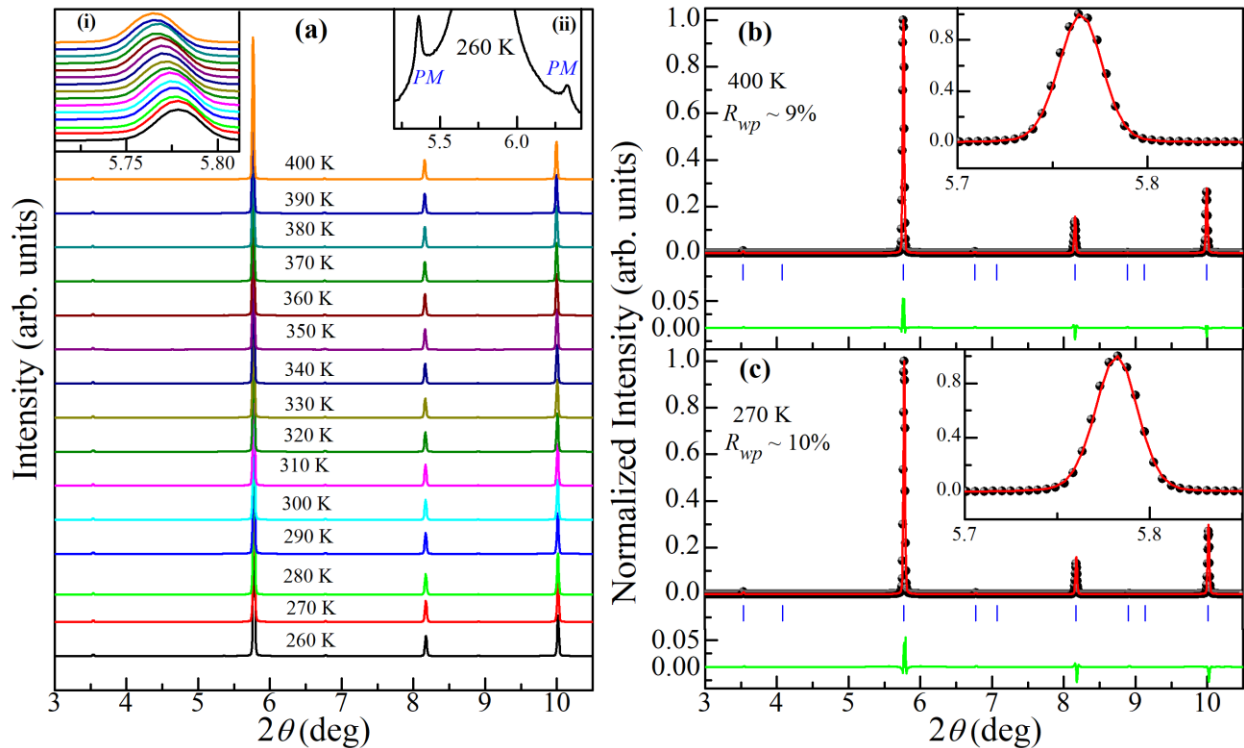

Figure 3.7: (a) High-resolution SXRPD patterns at various temperatures in the temperature range 260 K to 400 K. The inset (i) shows the enlarged view around the most intense Bragg peak of the cubic austenite phase at various temperatures while the inset (ii) depicts a highly magnified view around the most intense peak at 260 K showing the appearance of satellite peaks corresponding to the premartensite phase, which are marked as "*PM*". The panels (b) and (c) show the observed (black circles), calculated (continuous red line), and difference profiles (continuous green line at the bottom) obtained after Rietveld refinement using SXRPD data at 400 K and 270 K,

respectively, while the blue tick bars indicate the Bragg peak positions and R_{wp} is the weighted agreement factor. The inset in (b) and (c) show the quality of Rietveld fit around the most intense peak.

Since the Rietveld refinements using the SXRPD data reveal the absence of any structural phase transition around T_C, the change in the unit cell volume in the FM cubic austenite phase with respect to that in the paramagnetic cubic austenite phase suggests the presence of magnetoelastic coupling across T_C. The extrapolation of linear volume expansion region of the paramagnetic cubic austenite phase, shown with the blue line in Figure 3.8(a), to the FM cubic austenite phase region (i.e., $T_{PM} < T < T_C$) reveals that the cubic unit cell volume undergoes substantial contraction below T_C in the FM cubic austenite phase. Taking into account the presence of magnetoelastic terms, the Landau free energy functional for the FM transition can be written as [264, 265, 302] :

$$\Delta G = \frac{1}{2}AM^2 + \frac{1}{4}BM^4 + \frac{1}{6}CM^6 + \frac{1}{2}kx^2 + QxM^2 \dots (3.2),$$

where $A = a_0 (T - T_C)$ with a_0 being a temperature-independent constant. The first three terms in eq. (3.2) correspond to the usual even powers of the order parameter (M) with temperature dependent coefficients B and C. The 4th term ($\frac{1}{2}kx^2$) is the elastic energy term, where k is force constant and x is the strain. The last term is the quadratic coupling term between strain and magnetization, with Q as the coupling coefficient. With a_0 and C as positive definite, the sign of the coefficient B decides the order of the phase transition [265, 302]. On taking the first derivative of ΔG w.r.t x and considering minimum stress condition in the material i.e., $\frac{\partial \Delta G}{\partial x} = 0$, the following quadratic (magnetostrictive [303]) relationship between the strain and the order parameter is obtained [265]:

$$x = -\frac{QM^2}{k} \dots (3.3)$$

77

On eliminating the strain term (x) using the above relationship, eq. (3.2) takes the form:

$$\Delta G = \frac{1}{2}AM^2 + \frac{1}{4}(B - 2Q^2/k)M^4 + \frac{1}{6}CM^6 \dots \text{ (3.4)}$$

Evidently, the magnetoelastic coupling term ($\frac{1}{2}QxM^2$) in eq. (3.2) renormalizes the coefficient of

the M^4 term. If $\frac{2Q^2}{k} > B$, the renormalized coefficient of M^4 becomes negative, and eq. (3.4) leads

to a first-order phase transition [265, 304]. Thus, the experimentally observed first-order character

of the paramagnetic austenite to FM austenite phase transition is essentially due to the emergence

of the magnetoelastic coupling in the Ni$_2$MnGa.
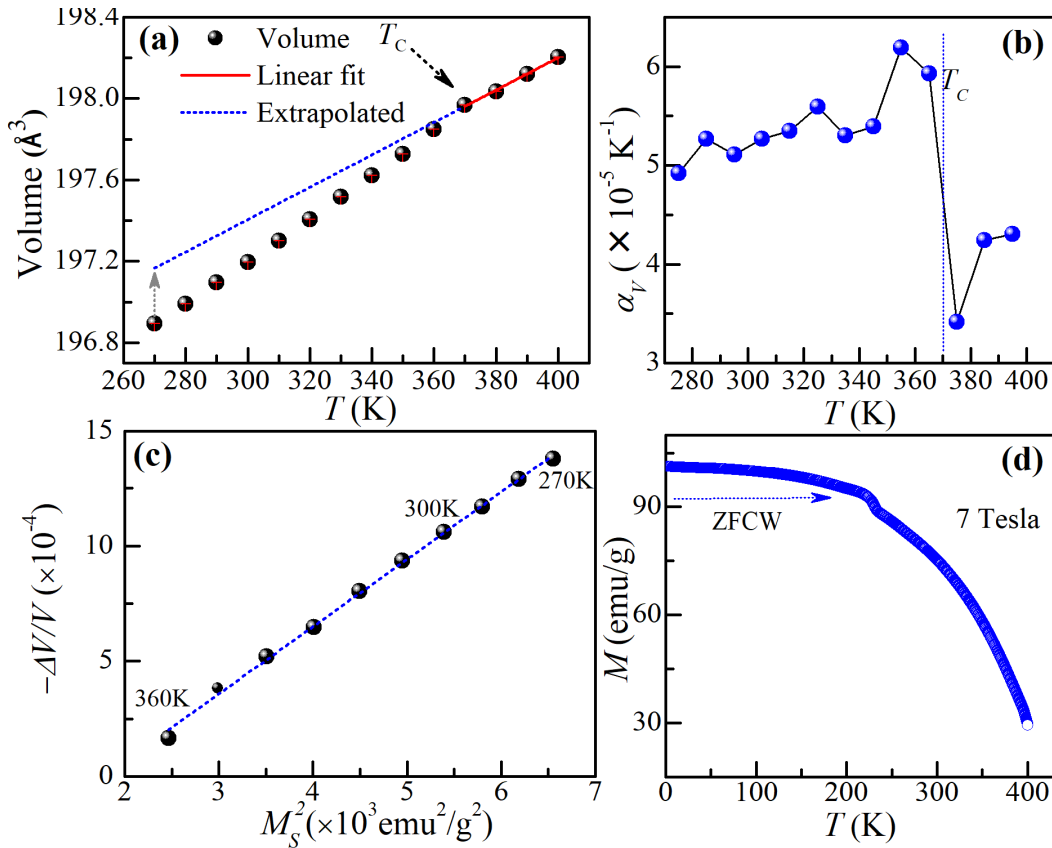

Figure 3.8: The variation of the (a) unit cell volume (V) with temperature showing volume
contraction at $T \leq T_C$, (b) linear volume expansion coefficient (α_V), obtained using the V versus T
plot, (c) cubic volume strain ($\Delta V/V$) with M_s^2 in the temperature range of 260 K $< T <$ 370 K, and

(d) spontaneous magnetization M_s, measured at 7 Tesla field, as a function of temperature. The dotted line (blue) in (a) is the extrapolated region of the linear expansion behavior above T_C, while the dotted line in (c) corresponds to the least-squares linear fit.

The change in the unit cell volume (ΔV) is calculated at each temperature below T_C in the FM region with respect to the extrapolated volume in the cubic paramagnetic region. The cubic volume strain ($\Delta V/V$) so obtained is found to scale quadratically with respect to the magnetization of the FM phase, as can be seen from Figure 3.8(c), where the magnetization was obtained using high field (7 Tesla) magnetization measurements as a function of temperature shown in Figure 3.8(d). At such a high field, one captures the spontaneous magnetization (M_S) of the Ni_2MnGa [305]. The quadratic dependence of $\Delta V/V$ on M_S is in agreement with eq. (3.3) that follows from the Landau free energy functional with the quadratic magnetoelastic coupling term in eq. (3.2). This quadratic dependence of volume and longitudinal strain on magnetization has been termed as magnetovolume effect [261, 262] and magnetostriction [303], respectively, in the literature.

3.4.4   Temperature dependent atomic pair distribution function analysis

Rietveld refinement captures the average long-range ordered (LRO) structure based on the Bragg peaks only and ignores the diffuse scattering. It cannot, therefore, capture the deviations from the LRO structure at short length scales of the order of one to a few unit cells, which contribute to the diffuse scattering. An understanding of the emergence of such short-range correlations can provide microscopic insight into the emergence of magnetoelastic coupling in the cubic austenite phase. To explore both the short-range ordered (SRO) and LRO structure together, we decided to use the atomic pair distribution function (PDF) [270-273] technique using high flux, high energy and high-Q synchrotron x-ray data, the details of which will be presented in this section. The PDF has information not only about the short-range regime (within the one unit cell or so) but also the

medium range (limited to a few unit cells) and long-range (above the medium range in real space) regimes [306, 307].
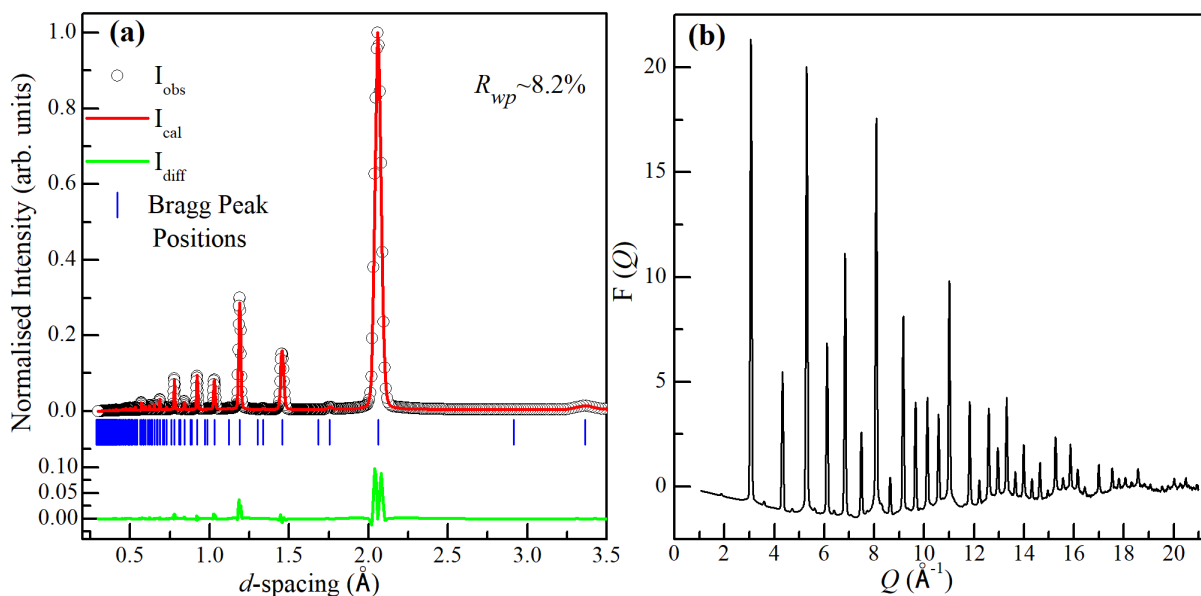

Figure 3.9: (a) The observed (black circles), calculated (continuous red line) and difference profiles (green line), Bragg peak positions (blue ticks), and weighted agreement factor (R_{wp}) obtained after Rietveld refinement of the cubic austenite phase in the $Fm\bar{3}m$ space group using high-Q SXRPD data at 400 K. (b) The reduced structure function $F(Q)$ versus Q.

The results of the Rietveld refinement using high-Q data at 400 K using the average cubic austenite structure are shown in Figure 3.9(a), which shows an excellent fit between the observed and calculated peak profiles by accounting for all the Bragg peaks. Figure 3.9(b) shows reduced structure function ($F(Q)$) with $Q_{max} = 21$ Å^{-1} at 400 K. It is important to note that the intensity of the peaks in the $F(Q)$ diminishes significantly towards higher Q values suggesting the dominance of the diffuse scattering. The corresponding reduced atomic PDF (i.e., $G(r)$) and its refinement at 400 K in the short-range (SR) regime are shown in Figure 3.10(a). There are several smaller

intensity peaks present below the first PDF peak corresponding to the shortest Ni-Mn/Ga pair around 2.52 Å.
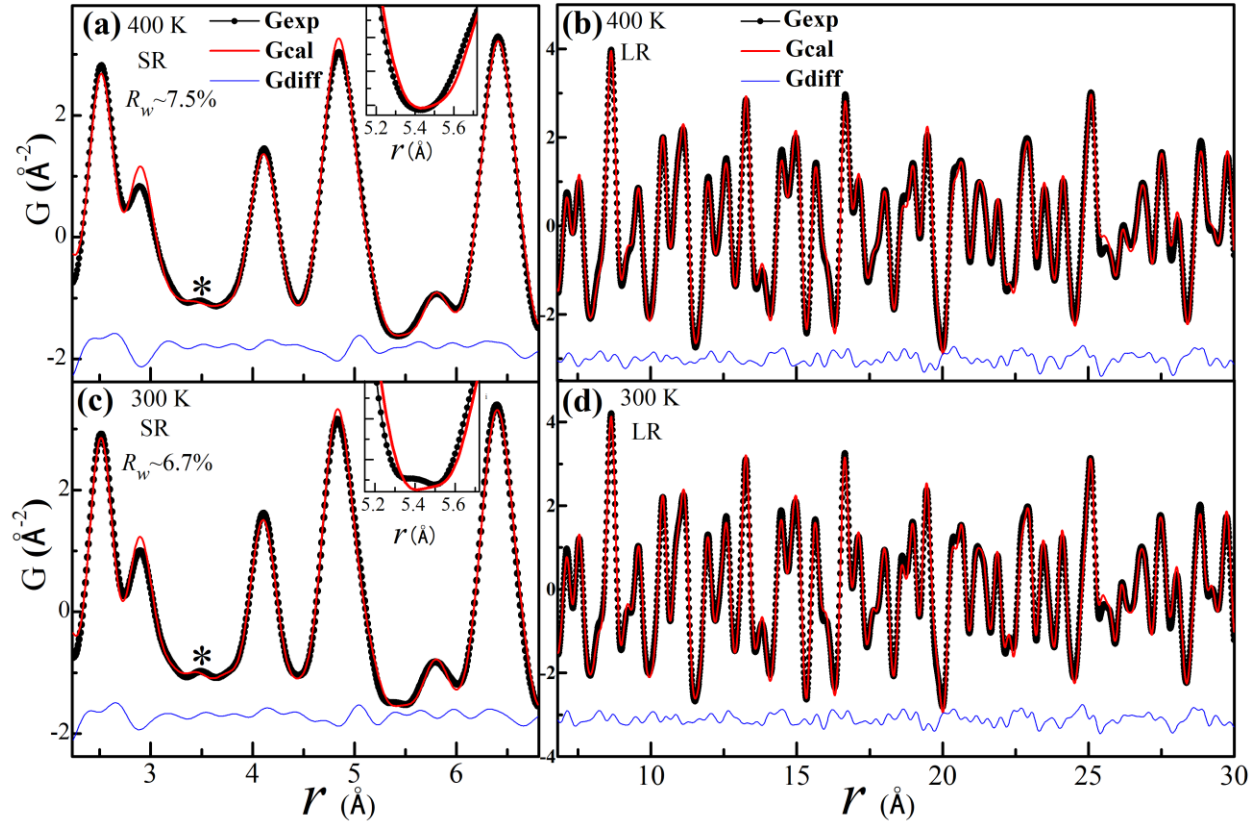

Figure 3.10: The experimental (dark black dots connect with black line) and calculated (continuous red line) PDFs and their difference (blue line at the bottom) obtained by real space structure refinement using cubic space group $Fm\bar{3}m$ in the (a) SR and (b) LR regimes at 400K, and (c) SR and (d) LR regimes at 300 K. The insets in (a) and (c) show an enlarged view of the PDF fits around 5.4 Å. The asterisk (*) marked peak is a ripple due to the truncation of the Fourier series.

These peaks appear during the Fourier transformation of the raw PDF data due to the truncation of the Fourier series to a limited Q value ($Q_{max} = 21$ Å^{-1}) and the background modeling [270, 273, 308]. These peaks do not correspond to any physical interatomic distances of the real space structure listed in Table 3.1 and are, therefore, considered as artifacts and hence not shown in Figure 3.10 [270, 273, 308]. The small peak around 3.5 Å marked with an asterisk (*) in Figure

3.10(a) and (c) also does not correspond to any physical pair of distances as per the crystallographic model listed in Table 3.1. In fact, the wavelength of the peak around 3.5 Å matches with the wavelength of the termination ripple $\lambda = 2\pi/Q_{max}$ [270], with $Q_{max} = 21$ Å^{-1}, This confirms that the PDF peak around 3.5 Å is a noise/ripple. This peak gets fitted in Figure 3.10 because the program PDFgui considers the effect of Fourier truncation ripples also in the refinement [274].

Table 3.1: Interatomic distances corresponding to the refined structural parameters of the austenite phase at 300 K and premartensite phase at 230 K reported in the literature [71].

Austenite Phase (*Fm$\overline{3}$m*)		Premartensite Phase (*Pnmn*)	
Atomic Pair	**Distance (Å)**	**Atomic Pair**	**Distance (Å)**
Ni-Mn and Ni-Ga	2.52206	Ni-Mn and Ni-Ga	2.50-2.53
Ni-Ni and Mn-Ga	2.91222	Ni-Ni and Mn-Ga	2.84-2.97
Ni-Ni, Mn-Mn and Ga-Ga	4.11851	Ni-Ni, Mn-Mn and Ga-Ga	4.08-4.15
Ni-Mn and Ni-Ga	4.82938	Ni-Mn and Ni-Ga	4.75-4.90
Ni-Ni and Mn-Ga	5.04412	Ni-Ni and Mn-Ga	5.04-5.0422
Ni-Ni, Mn-Mn and Ga-Ga	5.82445	Ni-Ni, Mn-Mn and Ga-Ga	5.75-5.88
Ni-Mn and Ni-Ga,	6.34705	Ni-Mn and Ni-Ga	6.28-6.39
Ni-Ni and Mn-Ga	6.51193	Ni-Ni and Mn-Ga	6.44-6.85

The peak positions in the real space *G(r)* (i.e., PDF) represent the pairs of atoms separated by a given distance *r,* and the peak width depends on the dynamic (thermal) and static disorder in the system [270, 309]. The PDF peak shape provides information about the atomic pair probability distribution, while the integrated intensity of the PDF peak is related to the coordination number [270-272]. All the PDF peaks in the short-range (SR) and long-range (LR) regimes shown in

Figure 3.10(a) and Figure 3.10(b), respectively, are well accounted for with the cubic structure in the $Fm\bar{3}m$ space group confirming the average cubic austenite structure at high temperatures (400 K) at all length scales. However, we note the discrepancies between the calculated and observed PDF corresponding to 2nd and 4th peaks centered around 2.9 and 4.9 Å, which correspond to the Ni-Ni, Mn-Ga and Ni-Mn/Ga, Ni-Ni, Mn-Ga pairs of interatomic distances, covering various neighbours in the austenite phase, respectively (Table 3.1). This misfit, as discussed later, is the first signature of local disorder in the SR regime even at a temperature as high as 400 K. The cubic lattice parameter obtained from the real space PDF refinement in the LR regime turns out to be a = 5.8258(4) Å at 400 K, which is in broad agreement with that obtained by the Rietveld refinement using the high-resolution SXRPD data at 400K. After refining the structure in real space using $Fm\bar{3}m$ space group at 400 K, we attempted to refine the structure using the experimental $G(r)$ at 300 K, assuming the same space group $Fm\bar{3}m$. Although the overall fit may appear satisfactory, it is evident from the inset of Figure 3.10(c) that there is a misfit between calculated and experimental PDFs around 5.4 Å. Further, the misfit between the calculated and experimental PDFs around the 2nd and 4th peaks persists, as at 400 K. On the other hand, the PDF fits in the LR region for $r \geq 6.8$ Å are quite good for the cubic structure, both at 400 K and 300 K, as can be seen from Figure 3.10(b) and Figure 3.10(d). This reveals that the structure in the LR regime remains cubic at 400 K and 300 K. However, the same structure gives rise to misfit between the calculated and the experimental PDF in the SR regime. The tiny peak around 5.4 Å, shown more clearly in the inset of Figure 3.10(c) on a magnified scale, is obviously due to the departure from the cubic structure in the SR regime. The parameters obtained by refinement of the PDF in the SR regime, assuming the cubic structure, are listed in Table 3.2 at 400 K and 300 K.
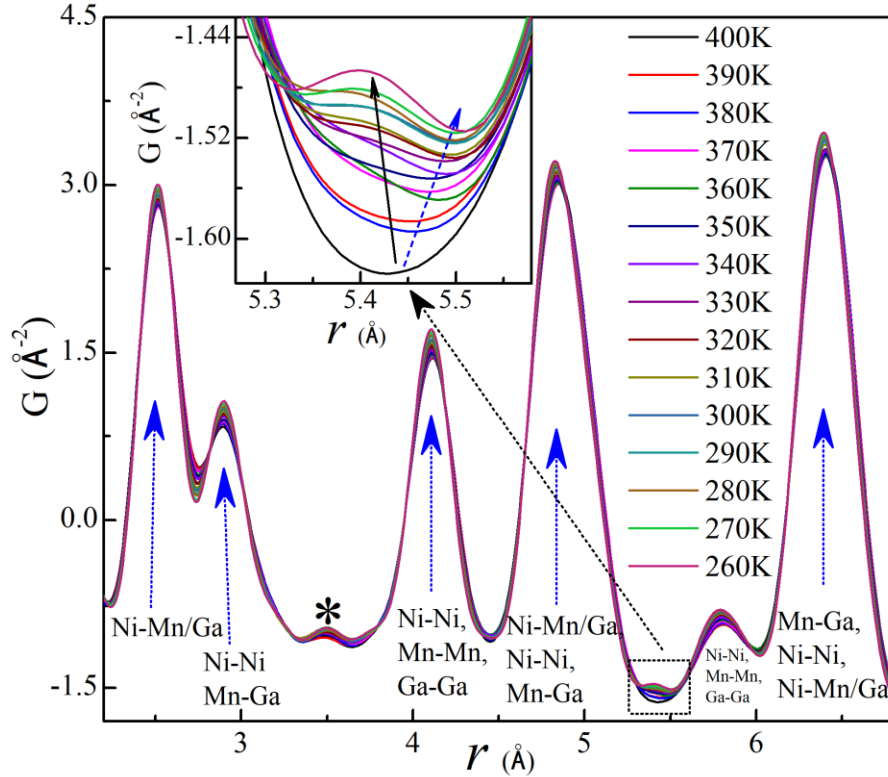
Figure 3.11: Experimental PDFs in the SR regime at various temperatures from 400 K to 260 K. The atomic pairs contributing to the individual peaks are indicated below the blue arrow line. The asterisk (*) marked peak is a ripple due to the truncation of the Fourier series. The inset shows an enlarged view around 5.4 Å, where the black arrow is to guide to the emergence of new pair of interatomic distance while the blue arrow shows the shift of the minima towards the higher r side.

To understand the evolution of the local structure in the SR regime, the atomic PDF in the temperature range 400 K to 260 K covering the austenite and the premartensite phase regions is depicted in Figure 3.11. The atomic pairs corresponding to the various peaks in the PDF are marked with arrows in Figure 3.11 based on the interatomic distances corresponding to the crystallographic model structure of the cubic austenite and 3M premartensite phases listed in Table 3.1 [71]. Although there are no major changes observed in $G(r)$ in the temperature range 400 K to 260 K (see Figure 3.11), the temperature dependent evolution of $G(r)$ around 5.4 Å, shown in the inset

of Figure 3.11, clearly reveals the emergence of a new peak. At 400 K, there is no such peak, but the shape of $G(r)$ begins to change on cooling below 400 K, especially around the T_C (~371 K). Further, below 340 K, the new PDF peak begins to appear. The change of shape of $G(r)$ followed by the emergence of this new peak around 5.4 Å on lowering the temperature suggests that this feature appears below T_C (~371 K). Below T_C, the minimum in the PDF shifts from around 5.45 Å towards higher r value, as shown schematically using the dotted blue arrow in the inset of Figure 3.11. Further, the position of the peak around 5.4 Å shifts to the lower r side with decreasing temperature, as shown by the solid black arrow in the inset of Figure 3.11, and the intensity of this peak grows with decreasing temperature up to 260 K, which is the austenite to premartensite phase transition temperature T_{PM} of Ni_2MnGa (see Figure 3.1). Since the peak position in the atomic PDF represents the atomic pairs separated at a given distance r for a given structure, the appearance of a new peak around 5.4 Å (see the inset of Figure 3.11) with the change in temperature is a signature of the emergence of new atomic pairs. This indicates that the peak around 5.4 Å might be related to the local premartensite structure.

To confirm the emergence of premartensite structure, first of all, the structure is refined using the experimental PDF data at 260 K, considering the *Pnmn* space group (commensurate model) [71] of the premartensite phase. The results of the refinement are shown in Figure 3.12(a) and Figure 3.12(b) in the SR and SR+LR regimes, respectively. All the PDF peaks are well accounted for, including the peak around 5.4 Å, which could not be accounted for at 300 K using the cubic austenite structure (Figure 3.10(c)). Further, the misfit around the 2nd and 4th PDF peaks (discussed in the context of Figure 3.10) has completely disappeared. All these indicate that the misfits around 2.9 Å and 4.9 Å and the appearance of an extra peak around 5.4 Å (Figure 3.10 and Figure 3.11), which started appearing in the PDF well above T_{PM} ($\simeq$260 K), are related to the premartensite

phase. The real space PDF refined structural parameters for 260 K PDF data in the SR regime are given in Table 3.2.
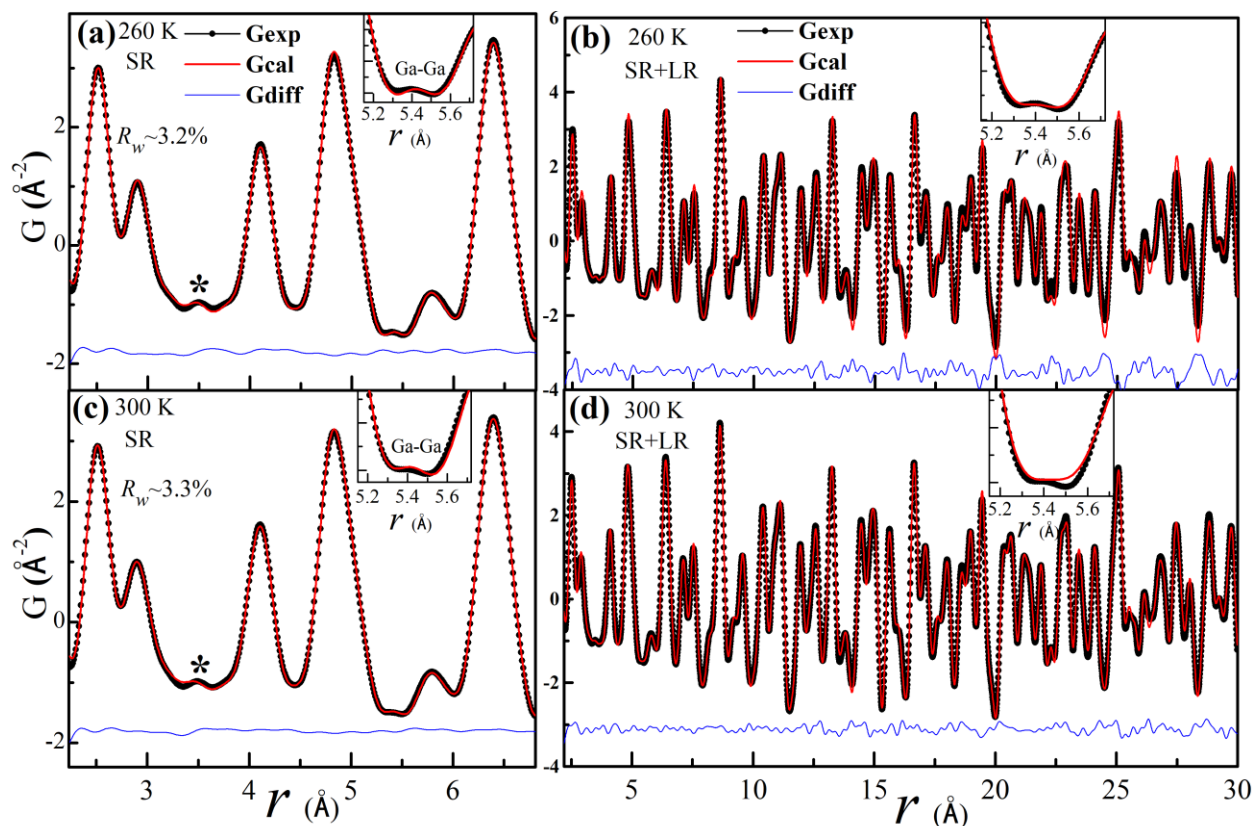

Figure 3.12: The experimental (dark black dots connected with black line) and calculated (continuous red line) PDFs and their difference (blue line at the bottom) obtained by real space structure refinement at 260 K using 3*M* modulated orthorhombic premartensite phase space group *Pnmn* in the (a) SR and (b) SR+LR regimes. The PDF fits at 300 K using the same space group (*Pnmn*) in the (c) SR and (d) the SR+LR regimes. The insets in (a), (b), (c), and (d) show an enlarged view of the PDF fit around 5.4 Å. The asterisk (*) marked peak is a ripple due to the truncation of the Fourier series.

After the PDF fitting, we found that the peak around 5.4 Å in PDF corresponds to the Ga-Ga atomic pair of the premartensite phase. The peak around 2.9 Å (2nd peak) corresponds to the Ni-

Ni and Mn-Ga, while the peak around 4.9 Å (4th peak) corresponds to the Ni-Mn/Ga, Ni-Ni and Mn-Ga pairs of the premartensite phase. The emergence of features related to the premartensite phase in the SR regime as a function of temperature is investigated.

Table 3.2: Parameters obtained from the PDF refinement using cubic austenite ($Fm\bar{3}m$) and $3M$ commensurate premartensite (*Pnmn*) structures in the SR regime at selected temperatures. The *a*, *b*, *c* are the lattice parameters, U_{iso} is the isotropic atomic displacements parameter, δ_2 is the coefficient for $1/r^2$ contribution to the peak sharpening, and R_w is the weighted agreement factor for the PDF refinement.

Parameters	Austenite phase refined		Premartensite phase refined	
	400 K	300 K	260 K	300 K
a (Å)	5.825 (6)	5.811 (5)	4.10 (1)	4.11 (1)
b (Å)	5.825 (6)	5.8117 (6)	5.80 (1)	5.805 (8)
c (Å)	5.825 (6)	5.8117 (6)	12.27 (3)	12.28 (1)
U_{iso} (Ni)	0.013 (1) Å^2	0.010 (1) Å^2	0.002 (1) Å^2	0.002 (1) Å^2
U_{iso} (Mn)	0.016 (3) Å^2	0.016 (3) Å^2	0.0003 (2) Å^2	0.0004 (2) Å^2
U_{iso} (Ga)	0.007 (2) Å^2	0.005 (1) Å^2	0.004 (2) Å^2	0.005 (3) Å^2
δ_2 (Å^2)	3.1 (0.4)	3.2 (4)	3 (1)	5.60 (2)
R_w (%)	7.5	6.7	3.2	3.3

Figure 3.12(c) and Figure 3.12(d) depict the fits between the calculated and experimental PDF after refinement at 300 K using the structure of the premartensite phase in the *Pnmn* space group in the SR and SR+LR regimes, respectively. The fits are excellent in the SR regime as can be seen from Figure 3.12(c). Interestingly, the extra peak around 5.4 Å is well captured with the premartensite structure model in the SR regime, as can be seen from the inset of Figure 3.12(c).

The refined parameters for the SR regime are listed in Table 3.2. Attempts to fit both the SR and LR regimes together at 300 K led to misfit for the peak around 5.4 Å, as can be seen from the inset of Figure 3.12(d). This clearly reveals that the signature of the premartensite phase is present only at SR length scales. In the LR regime, all the peaks at 300 K were well fitted using the cubic $Fm\bar{3}m$ space group (see Figure 3.10(d)). Our results thus provide unambiguous evidence for the existence of the premartensite structure at 300 K in the SR regime even though this temperature (300 K) is well above the actual premartensite transition temperature T_{PM} ($\simeq$260 K). The feature in the experimental PDF that appears below 370 K (Figure 3.11) itself confirms the precursor state of the premartensite phase within the austenite phase region. Our results are consistent with the observation of diffuse streaks due to such a precursor state in the austenite phase in the inelastic neutron scattering and high-resolution transmission electron microscope (HRTEM) studies [88, 118].

The length scale corresponding to the best fit to the experimental PDF is the correlation length (ξ) [264, 307] of the precursor state of the premartensite phase. To determine the ξ as a function of temperature, the range of r gradually varied up to which the experimental PDF could be fitted using the premartensite phase structure. Figure 3.13(a) to Figure 3.13(g) corresponds to the maximum distance in real space up to which premartensite phase structure is able to capture all the PDF peaks successfully along with the anomalous peak around 5.4 Å. On the other hand, Figure 3.13(h) to Figure 3.13(n) show that when the value of r exceeds the correlation length, a clear misfit around 5.4 Å is observed. The variation of ξ with temperature is shown in Figure 3.14, where the ξ of the LRO premartensite phase below $T_{PM} \leq 260$ K was determined from Scherrer equation [310] ($\xi = 0.9 \times \lambda/\beta \times \cos\theta$) using the experimental FWHM (β) of the premartensite phase peak in the high-resolution SXRPD patterns around $2\theta = 6.32°$. The instrumental broadening was

negligible as compared to the observed FWHM. The discontinuous behavior of ξ at 260 K with its saturation below 260 K, seen in Figure 3.14, clearly reveals the first-order nature of the austenite to premartensite transition temperature [66, 100]. The presence of the tail region above 260 K, where ξ grows very slowly as a precursor state of the premartensite phase with decreasing temperature, suggests that this transition is a fluctuation-driven first-order phase transition [311]. We find that ξ increases from $r \sim 7.4$ Å in the austenite phase region at 330 K to $r \sim 367$ Å at 230 K in the premartensite phase region. It is interesting to note that the ξ obtained by us above T_{PM} (~1 nm at 290 K) is comparable to the width of alternate dark and light bands (~1.2 nm at 293 K) in HRTEM images of the tweed microstructure, which is the characteristic feature of the precursor state of the premartensite phase in Ni_2MnGa [118]. The analysis of the experimental PDF thus reveals that the local structure of the cubic austenite phase corresponds to the precursor state of the premartensite phase, and that this precursor state appears well above T_{PM} as well as above the FM T_C. The presence of the precursor state of the premartensite phase in the SR regime of the austenite phase is responsible for the emergence of the magnetoelastic strains, observed in the FM austenite phase region, which in turn leads to the first-order character of the paramagnetic to FM phase transition due to the coupling of the FM order parameter with the magnetoelastic strains [63, 100]. Also, the local premartensite structure of the cubic austenite phase is responsible for the decrease in magnetization (Figure 3.1(a)) below T_C due to higher magnetocrystalline anisotropy energy of the premartensite phase in comparison to the cubic austenite phase [263].
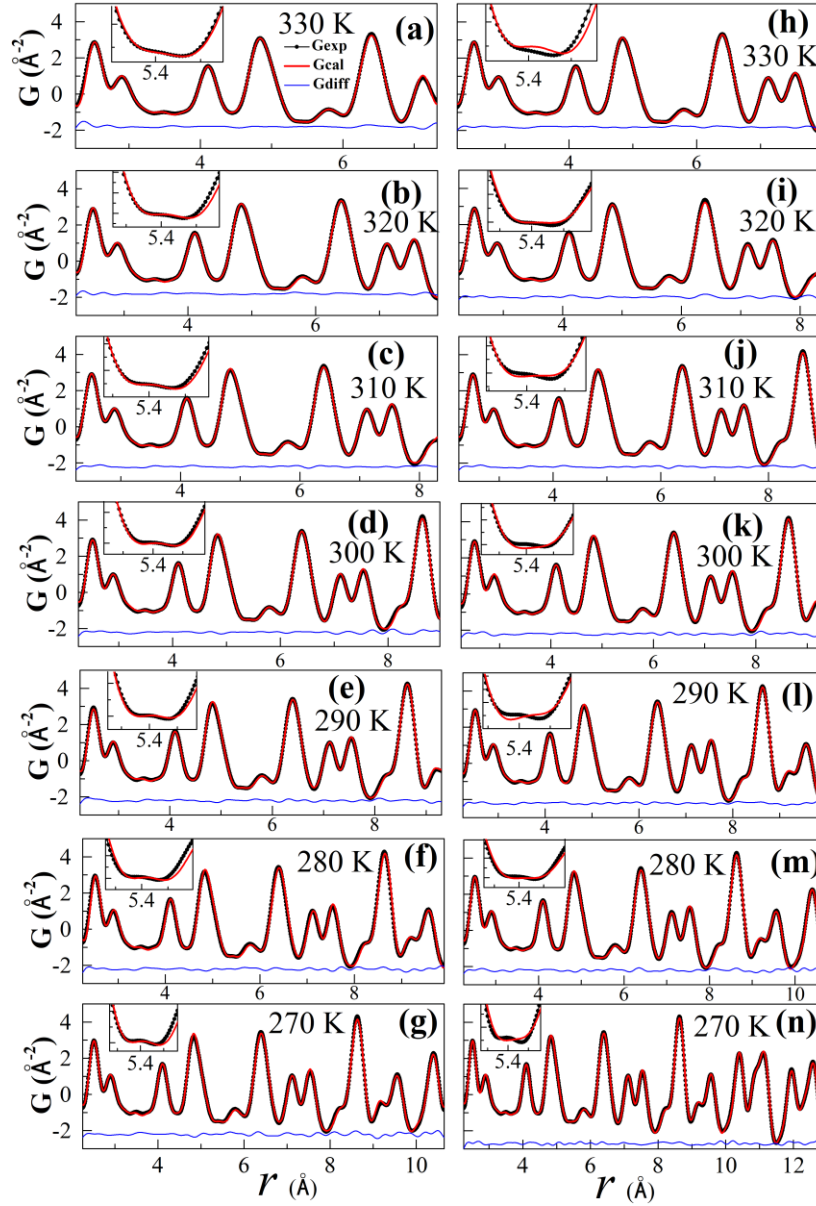
Figure 3.13: The experimental (dark black dots connected with black line) and calculated (continuous red line) PDFs and their difference (blue line at the bottom) using the 3*M* modulated orthorhombic premartensite phase space group (*Pnmn*) in the temperature range 330 to 270 K obtained by real space structure refinement. The left panel ((a) to (g)) shows fits up to the correlation length (ξ) for which the premartensite phase structure is able to account for the peak around 5.4 Å, as shown in the insets. The right panel ((h) to (n)) depicts the fits to a distance, which is greater than the correlation lengths. The misfit for the peak around 5.4 Å is quite evident from the insets of (h) to (n).
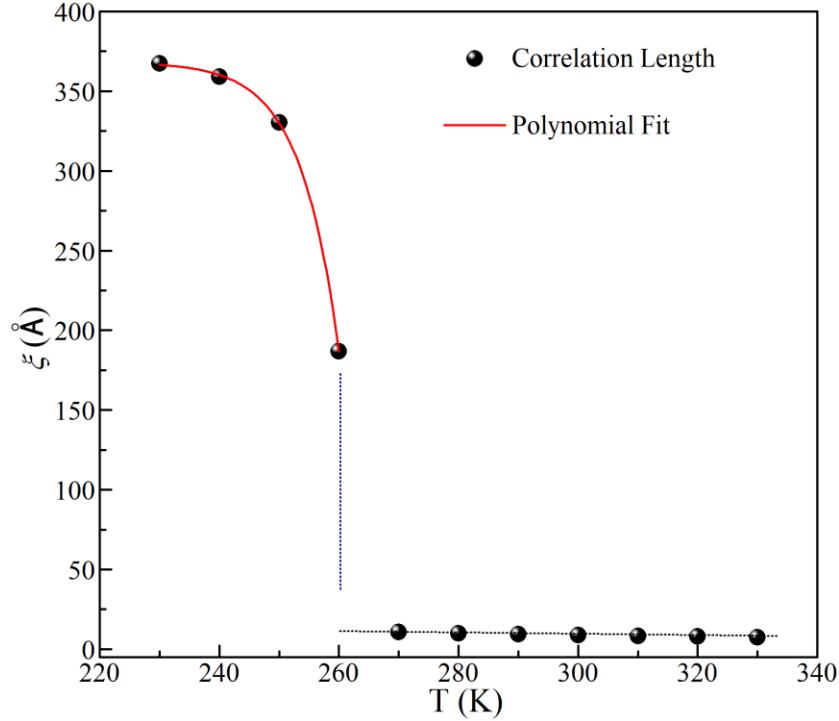
Figure 3.14: The correlation length (ξ) of the premartensite phase as a function of temperature. The black dotted line shows the slowly increasing trend of ξ in the temperature range 330 to 270 K. The sharp increase in ξ at T_{PM} ~ 260 K is shown by the dotted blue line. Below 260 K, ξ tends towards its saturation value for the long-range ordered premartensite phase.

3.5   Conclusions

To conclude, the evidence for the existence of the precursor state of the premartensite phase in the Ni$_2$MnGa MSMA by atomic pair distribution function analysis of the high-Q synchrotron x-ray powder diffraction data is presented here. Our results reveal that the local structure of the cubic austenite phase corresponds to the precursor state of the premartensite phase. The evidence for quadratic magnetoelastic coupling in the austenite phase arising from the presence of such SRO precursor state is also presented. Within the framework of the Landau theory, the coupling of the magnetoelastic strains with the FM order parameter around T_C imparts first-order character to the

paramagnetic to FM phase transition, as revealed by the thermal hysteresis in the FM T_C in the heating and cooling magnetization cycles. The presence of the local premartensite precursor state in the FM austenite phase also explains the anomalous reduction in the magnetization below T_C due to the higher magnetocrystalline anisotropy of the premartensite phase causing significant deviation from the $M \sim (T - T_C)^{1/2}$ type order parameter behavior expected for a second-order FM phase transition. The present findings significantly advance the understanding of the precursor state of the premartensite phase and its impact on the nature of paramagnetic to FM phase transition as well as the temperature dependence of the magnetization in the FM state of MSMAs in general and Ni_2MnGa in particular.